

Superconducting Higgs particle observed by non-equilibrium Raman scattering

Tomke E. Glier,^{1,*} Mika Rerrer,¹ Lea Westphal,¹ Garret Lüllau,¹ Liwen Feng,² Sida Tian,³ Jakob Dolgner,³ Rafael Haenel,³ Marta Zonno,^{3,4,5} Hiroshi Eisaki,⁶ Martin Greven,⁷ Andrea Damascelli,^{4,5} Stefan Kaiser,^{8,†} Dirk Manske,^{3,‡} and Michael Rübhausen^{1,§}

¹*Institute of Nanostructure and Solid State Physics,
Universität Hamburg, Hamburg, 22761, Germany.*

²*Institute of Solid State and Materials Physics, TUD Dresden University of Technology, Dresden, 01062, Germany.*

³*Max Planck Institute for Solid State Research, Stuttgart, 70569, Germany.*

⁴*Quantum Matter Institute, University of British Columbia, Vancouver, BC V6T 1Z4, Canada.*

⁵*Department of Physics & Astronomy, University of British Columbia, Vancouver, BC V6T 1Z1, Canada.*

⁶*Nanoelectronics Research Institute, National Institute of Advanced
Industrial Science and Technology, Tsukuba, Ibaraki 305-8568, Japan.*

⁷*School of Physics and Astronomy, University of Minnesota, Minneapolis, MN, USA.*

⁸*Technical University of Dresden, Faculty of Physics,
Institute for Solid State and Material Physics, 01062 Dresden, Germany*

(Dated: February 16, 2024)

Even before its role in electroweak symmetry breaking, the Anderson-Higgs mechanism was introduced to explain the Meissner effect in superconductors.[1, 2] Spontaneous symmetry-breaking yields massless phase modes representing the low-energy excitations of the Mexican-Hat potential. Only in superconductors does the gauge field move the phase mode towards higher energies, as a consequence of the charged condensate. This results in a low-energy excitation spectrum governed by the amplitude mode - the Higgs mode.[3] Consequently, the Meissner effect signifies a macroscopic quantum condensate in which a photon acquires mass, representing a one-to-one analogy to high-energy physics.[4, 5] We report on the direct observation of the Higgs particle in the high-temperature superconductor Bi-2212 by developing an innovative technique to study its distinct symmetries and energies after a soft quench of the Mexican-Hat potential.[6] By comparing transient Stokes and anti-Stokes data, we identify the Higgs particle as an additional anti-Stokes Raman cross section after quenching. With our technique we discriminate quasi-particle excitations from excitations in the Cooper channel and argue that alternatives to the Higgs excitation can be ruled out. This opens the avenue for Higgs Spectroscopy in quantum condensates and provides a unique pathway to control and explore Higgs physics.

The Higgs mode is a Raman-active excitation, and was observed in NbSe₂ in 1980 by R. Sooryakumar and M.V. Klein.[7] The microscopic nature of this discovery was pointed out much later by Y. Nambu to P. Higgs, and was seen by both as a first observation of the Higgs mode in experimental physics.[4] However, the Raman cross section of the Higgs mode in superconductors is generally very small, resulting in Higgs modes that remain invisible in most Raman experiments. In NbSe₂, a unique interplay between a soft phonon in the charge-density wave state and the Higgs mode in the superconducting (SC) state leads to a dedicated and sharp mode slightly below 2Δ . [8–10] This interplay was intensively studied as a function of temperature and pressure.[11, 12] Very recently, the coupling between charge-density wave and Higgs mode was also studied by time-resolved spectroscopy of phase- and amplitude-resolved high harmonics.[8, 13] Up to now, the observation of the Higgs mode in Raman scattering has been limited to this particular case, since in non-charge-density-wave systems the Mexican-Hat potential must be specifically quenched, for instance by a light pulse.[14]

In previous works, spontaneous Raman spectroscopy on high-temperature superconductors has been explored

with regard to excitation-energy resonances and the dynamics of the SC gap feature. Static Raman spectra of Bi₂Sr₂CaCu₂O_{8+ δ} (Bi-2212) in B_{1g} symmetry show distinct resonances between 2 eV and 3.5 eV indicating a multicomponent origin of the excitation spectrum close to 2Δ . [15] Furthermore, transient time-resolved Raman scattering in the SC state enables the study of pair-breaking excitations and the dynamics of the SC order parameter. Bi-2212 shows different picosecond dynamics of the components of the excitation spectrum in the SC state.[16] By utilizing the Bose factor, time-resolved Stokes-anti-Stokes Raman scattering has been applied as a stroboscopic tool to determine transient temperatures and melting processes in highly excited states of phonons.[17, 18]

Advances in THz-laser technology have enabled the investigation of Higgs modes in several classes of superconductors via non-equilibrium THz spectroscopy.[14, 19–26] These experiments involve either an impulsive excitation of the Higgs mode based on a *quench* of the SC state or a *drive* of the Higgs mode, resulting in coherent oscillations or high-harmonic generation, respectively. The theoretical models are based on time-dependent Ginzburg-Landau approaches and time-dependent BCS theories in

the framework of a pseudospin model.[21, 27–29] The important influence of disorder and impurity effects on high-harmonic generation was investigated from a theoretical point of view.[30–32] Furthermore, the SC state exhibits a manifold of low-energy excitations, such as pair breaking, Josephson plasmons, Bardasis-Schrieffer, or Leggett modes.[33–36] Some of them are very difficult to distin-

guish from the Higgs mode in an experimental data set. Thus, it is of great importance that the Higgs mode can be classified based on the symmetry of the SC condensate, by the symmetry of the quench, and the symmetry of the Higgs excitation.[6] This diversity of experimental parameters enables the control and exploration of Higgs physics in an unprecedented way.

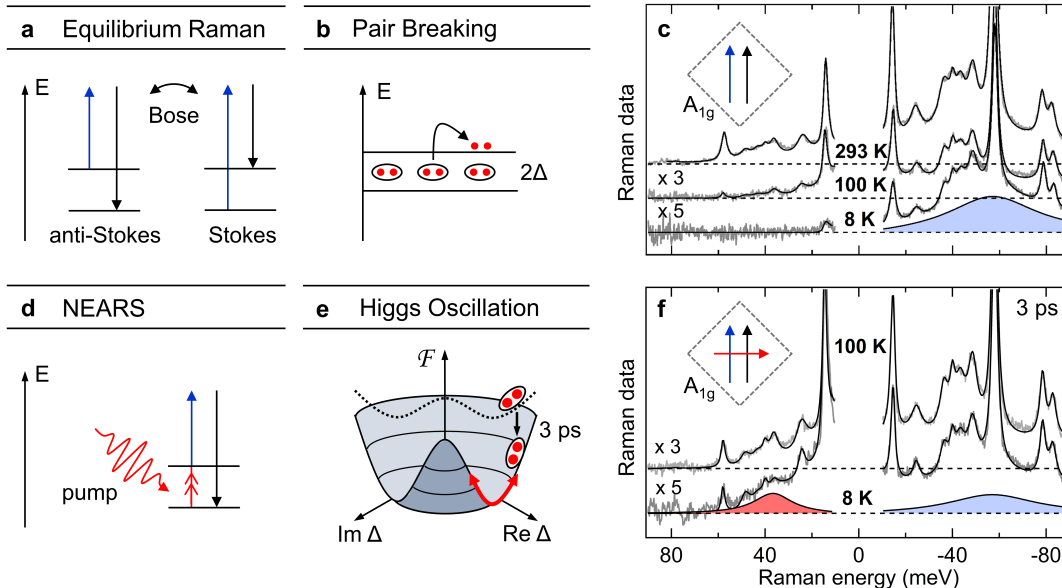


FIG. 1. Equilibrium vs. non-equilibrium Raman scattering. (a) The energy diagrams of equilibrium Stokes (energy-loss) and anti-Stokes (energy-gain) scattering are linked by the Bose function. The thermal factors of Stokes and anti-Stokes scattering link Raman susceptibilities to Raman intensities. The Raman probe excitation is depicted in blue, the scattered light is shown in black. (b) The Raman response is dominated by pair-breaking of Cooper pairs. (c) Stokes and anti-Stokes equilibrium Raman data of Bi-2212 ($T_c = 92$ K[37], see Fig. S3) in a scattering configuration of A_{1g} symmetry at indicated base temperatures. The measured intensities are shown in gray, and the black solid lines represent fits to the measured intensities (see SI, Fig. S5). The pair-breaking feature susceptibility is highlighted in blue (filled). The anti-Stokes Raman spectrum at 8 K is vanishing. (d) After a pump (red wiggly line), the excited Higgs mode (red double arrow) can be detected by an annihilation process that is visible in the anti-Stokes data. (e) The modification of the free-energy landscape (dotted line) induced by the pump enables the annihilation of the Higgs oscillations (solid red line). (f) Pump-probe Stokes and anti-Stokes Raman spectra in A_{1g} symmetry at indicated temperatures above (upper spectra, fluence $59 \mu\text{J cm}^{-2}$) and below T_c (lower spectra, fluence $113 \mu\text{J cm}^{-2}$) at a time delay of 3 ps. Below T_c , at 8 K base temperature, the anti-Stokes intensity cannot be modelled via the Stokes susceptibility and a new NEARS feature occurs (see Fig. S6), which we attribute to the A_{1g} Higgs mode. The susceptibility of the NEARS feature is highlighted in red (filled).

Non-Equilibrium Anti-Stokes Raman Scattering

Here we resolve the ambiguity of the identification of Higgs modes in superconductors by introducing a new spectroscopic technique: Non-Equilibrium Anti-Stokes Raman Scattering (NEARS) - see Figure 1. NEARS measures the spontaneous Raman scattering signal, which is proportional to a four-photon Greens function where Stokes and anti-Stokes signals are generated simultaneously after the quench of the Mexican-Hat potential. The Higgs excitations that result from the relaxation process of the free-energy landscape yield an overpopulated state (see also Fig. S9). This imbalance can be measured by a comparison between the simultaneous Stokes and anti-

Stokes signals i.e. energy-loss and energy-gain data of the spontaneous Raman process.

Conventional Raman scattering generates excitations leading to energy-loss spectroscopic features on the Stokes side (see Fig. 1a-c). In superconductors, this technique is sensitive to low-energy excitations, such as pair-breaking excitations[38, 39], see Fig. 1b and c, density correlation functions of Josephson plasmons[35], Leggett modes[40], and Bardasis-Schrieffer modes[41, 42]. Our aim is to measure the relaxation of a superconductor and the concomitant generation of Higgs modes in the quasi-static limit and in nearly thermal equilibrium, i.e. under the condition of a soft quench (Fig. 1d-f).

In this work, NEARS is applied to the high-temperature superconductor Bi-2212 (slightly under-

doped, $T_c = 92$ K, see SI Fig. S3).[37] To ensure the condition of quasi-equilibrium in the non-pumped data, we use the fact that Stokes and anti-Stokes scattering intensities in equilibrium are linked by the Bose function. We measure the Stokes data as a function of temperature and calculate the corresponding anti-Stokes response. Matching Stokes and anti-Stokes spectra over a large low-energy range ensures that we have determined the temperature of the sample under laser illumination, excluded any background artifacts from the pulsed laser source, and avoided unwanted self-excitation effects induced by the pulsed Raman probe (see Fig. S5 and S8). Indeed, in Fig. 1c, a perfect agreement between the calculated and measured anti-Stokes data is observed when assuming a heating of 9 K due to the Raman probe. We apply a scattering geometry that probes A_{1g} symmetry with incidence and scattered light fields parallel to each other and rotated 45° to the CuO_2 plane of Bi-2212, as indicated in the inset. An incident photon energy of 3 eV (400 nm), a laser power of 4.8 mW, and a pulse duration of 1.2 ps were used. In the SC state, at low temperatures, and on the Stokes side, we observe the well-known phonons and excitations around twice the SC gap energy (2Δ) due to the predominant pair-breaking process at 60 meV of Bi-2212 as expected for a sample with $T_c \approx 92$ K. The pair-breaking process is sketched in Fig. 1b.[15, 43] The excitation at around 2Δ is a composite feature as seen by resonant Raman scattering with excitation energies in the UV spectral range.[15] The anti-Stokes side is essentially dark due to the suppression of the Raman response as no excitations are thermally excited at $T \approx 0$ K and, hence, no annihilation of excitations can occur (see 8 K data in Fig. 1c).

The NEARS experiment is illustrated in Fig. 1d. The pump that excites the sample allows us to choose pump geometries independent from probe geometries and control the strength of the soft quench by changing the fluence. This soft quench of the Mexican-Hat potential leads, after relaxation, to a specific Higgs mode excitation which has the form of an oscillation as shown in Fig. 1e. In the normal state (Fig. 1f, upper spectra), with a pump (1.2 ps, 1.55 eV (800 nm)) orthogonal to the Raman probe polarizations and with a time delay of 3 ps between pump and probe, we can still apply the quasi-equilibrium approach. We can calculate from the measured Stokes spectra the measured anti-Stokes data by using an additional pump heating of 3 K/mW (see Fig. S8). However, this approach fails in the SC state (Fig. 1f, lower spectra, see also Fig. S6). The additional cross section on the anti-Stokes side can be assigned to the Higgs mode after the pump-induced quench. Its energy at about 35 meV in A_{1g} symmetry corresponds to the frequency of the oscillation in the Mexican-Hat potential (see Fig. 1e). Its susceptibility is indicated in red in Fig. 1f. This feature is solely present on the anti-Stokes side, while on the pumped Stokes side we can identify a

persistent suppressed pair-breaking peak clearly indicating that the sample is still in its SC state 3 ps after the pump.

Fluence dependence of NEARS data

Figure 2 presents the fluence dependence of the Higgs modes excited in Bi-2212 at 8 K and at 3 ps delay. Two main symmetry configurations of the probe, corresponding to A_{1g} and B_{1g} , as shown in the insets of Fig. 2, are applied. The dashed squares mark the orientation of the CuO_2 planes. The pump is applied along the diagonals of the CuO_2 planes and carries a non-zero in-plane momentum due to its incidence angle of 21.8° (see Fig. S2).[44] In this configuration, one expects Higgs modes in both B_{1g} and A_{1g} probe symmetries.[6] Furthermore, the phonons allow an exact determination of the effective spot temperatures and, accordingly, the calculation of the Stokes and anti-Stokes thermal factors, which are relevant for fitting the NEARS data (see SI and Fig. S8).[45] The simultaneous fits to Stokes and anti-Stokes responses allow us to discriminate excitations around 2Δ from NEARS features below 2Δ (see Fig. S6). The latter are the consequence of the relaxation of the free-energy landscape. On the Stokes side, one can clearly see that the excitations around 2Δ in both B_{1g} and A_{1g} Raman probe symmetry get suppressed with increasing fluence, but remain non-zero even at the highest fluence, which demonstrates that Bi-2212 remains in the SC state. On the other hand, the feature on the anti-Stokes side around 35 meV in A_{1g} symmetry increases in intensity. We associate this with the enhanced population of the Higgs mode as a consequence of the increased strength of the soft quench. In B_{1g} symmetry, we find the Higgs mode at slightly lower energies around 30 meV and to broaden at higher fluences. In Fig. 2c, we show the integrated susceptibility of the Higgs modes and the pair-breaking excitation as a function of fluence. In both probe symmetries, we find a linear increase of the Higgs mode susceptibility and a concomitant decrease of the pair-breaking excitation. Furthermore, the A_{1g} Higgs mode increases more strongly than the B_{1g} Higgs mode. Fig. 2d shows the fluence dependence of the symmetry-dependent excitation energies. On the anti-Stokes side, the energy window, which allows an experimental observation of excited states, is limited by thermal factors (see Fig. S4). This energy window is indicated in Fig. 2d. Taking this into account, we conclude that the energy of the Higgs modes is only weakly dependent on fluence and that the A_{1g} feature occurs at higher energies compared to the B_{1g} feature. This behavior is in line with predictions for the Higgs particle.[6]

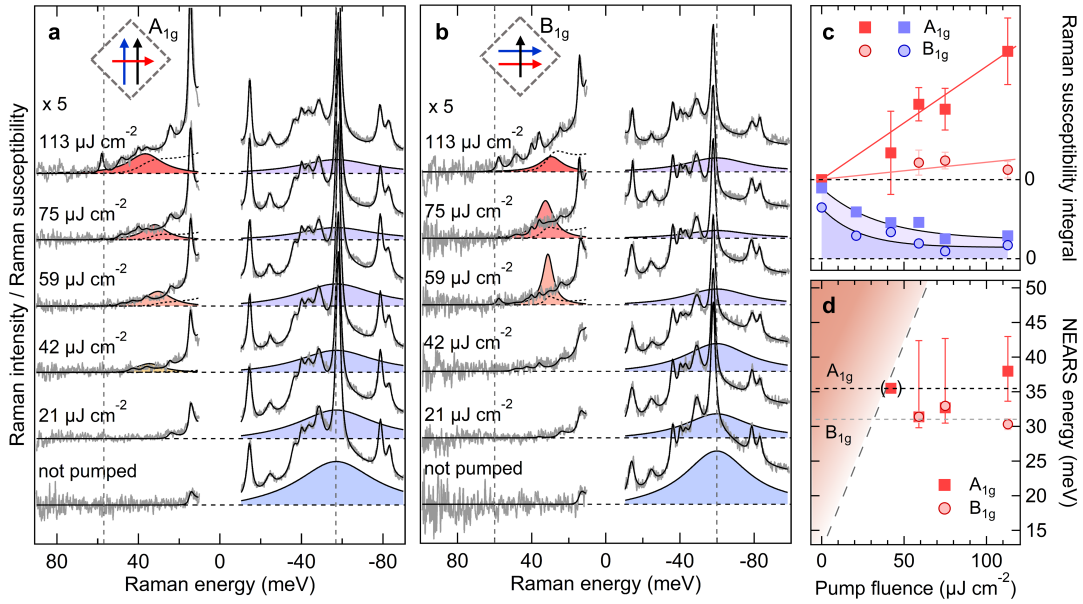


FIG. 2. Higgs particle as a function of fluence. Pump-probe Stokes and anti-Stokes Raman spectra at 8 K and a time delay of 3 ps for fluences between 0 $\mu\text{J cm}^{-2}$ (not pumped) and 113 $\mu\text{J cm}^{-2}$. (a) A_{1g} and (b) B_{1g} geometry. Anti-Stokes Raman intensities are multiplied with a factor of 5 for better visibility. The pair-breaking peak on the Stokes side is highlighted in blue, whereas in the anti-Stokes spectra the new NEARS feature (Higgs modes) susceptibility is clearly visible at fluences larger than 50 $\mu\text{J cm}^{-2}$ and marked in red. The dashed vertical lines mark the position of the pair-breaking feature on the energy-gain and energy-loss side. (c) Integrated Raman susceptibility of the Higgs modes (red) and of the pair-breaking peak (blue) as a function of fluence. The solid lines represent guides to the eye (d) Excitation energy of the Higgs modes as a function of fluence. The anti-Stokes spectrum is limited at higher energies due to thermal Bose factors of the Raman intensity (see also Fig. S4). This is depicted as red-shaded area.

Excitations of the Higgs particle

The simultaneous measurement of excited energy-loss and energy-gain information allows us to create a unified NEARS map of the excitation landscape in the SC state of Bi-2212. Figure 3 is a superposition of the fluence-dependent superconductivity-induced excitations from both the Stokes and anti-Stokes spectra in A_{1g} and B_{1g} symmetry, respectively, identifying the A_{1g} and B_{1g} modes of the Higgs particle. Please note that the Stokes excitation spectrum covers the complete energy range shown, whereas the anti-Stokes side is limited to an energy range below the white dashed line due to the involved thermal factors (see Fig. S4 and S7). The non-quenched energy landscape is dominated by excitations around 2Δ . [35, 38] With increasing fluence, the 2Δ excitations gradually weaken, but remain at constant energy, indicating that Bi-2212 remains in its SC state. The A_{1g} excitation of the Higgs particle is an in-gap excitation at about 0.6 2Δ and increases in strength with fluence, showing a broadening at the highest fluence. The B_{1g} Higgs-particle excitation appears at about 0.5 2Δ . As a function of fluence it is more susceptible to the pump-weakening at the highest fluence. The symmetry of the associated Higgs modes for the given pump/probe configuration are indicated in both panels.

Higgs particle and other SC excitations

The Hamiltonian describing a superconductor has two contributions $H = H_{\text{BCS}} + H_1$ with

$$H_{\text{BCS}} = \sum_{\mathbf{k}} \Psi_{\mathbf{k}}^\dagger (\xi_{\mathbf{k}}\tau_3 + \Delta_{\mathbf{k}}\tau_1) \Psi_{\mathbf{k}} \quad (1)$$

showing a resemblance to the Dirac-equation in Nambu-spinor notation, and particle-hole symmetry (see SI). [1, 3, 5, 46, 47] The eigenvalues of H_{BCS} are $\pm E_{\mathbf{k}} = \pm\sqrt{\xi_{\mathbf{k}}^2 + \Delta_{\mathbf{k}}^2}$. Importantly, τ_1 yields an off-diagonal component to the Hamiltonian representing the quantum condensate of the superconductor. It is important to note that the corresponding Hamiltonian of, for instance, a charged-density wave system has no off-diagonal contribution. [10] H_{BCS} is modified by the Coulomb interaction of charged particles encoded in H_1 as pointed out by Anderson and Nambu. [1, 2, 5] This is a requirement for the Anderson-Higgs mechanism since it lifts the energy of the phase mode to the plasma frequency. In this case, the gap Δ acts as the mean-field expectation value of the Higgs field mediating mass to the electromagnetic gauge field, i.e. the photon, resulting in the Meissner effect. In contrast to high-energy physics, the expectation value and symmetry properties of the SC Higgs field are material-dependent and tunable. In high-temperature superconductors Δ has d-wave symmetry,

which opens the avenue to compare the excitation of the Higgs particle in different symmetries of the SC condensate and the quench. This allows to develop Higgs physics as we can compare theoretical prediction directly with the experiments.[6, 36]

We now discuss our results in the context of the Higgs mode and how it can be discriminated from alternative excitations of the superconductor. The important candidates are the pair-breaking (quasi-particle) excitations, the Josephson plasmon modes, and the Bardasis-Schrieffer modes. *Pair-breaking excitation:* This is the dominant feature on the Stokes side of the spectra. It occurs due to the breaking of Cooper-pairs and generates quasi-particles in the single-particle channel, i.e. holes in Bi-2212 (see Fig. 1b). It is symmetry-dependent due to the inherent Coulomb screening, which is fully symmetric and affects only the A_{1g} channel, reducing the A_{1g} susceptibility and shifting the excitation to lower energies compared to B_{1g} symmetry (see Fig. 2a and b). However, for the NEARS feature we observe the opposite: The A_{1g} NEARS excitations exhibit a higher intensity and energy than in B_{1g} symmetry. Furthermore, the NEARS features appear as in-gap excitations. Therefore, they cannot be associated with pair-breaking excitations. *Excitations of in-plane Josephson plasmon modes:* They exhibit A_{1g} and B_{1g} symmetry.[34] However, we would expect the Josephson plasmon to exhibit an excitation energy that shifts to zero frequency as we increase the pump fluence.[34] Even our strongly-pumped A_{1g} data do not show this behavior. Therefore, they can be ruled out as well. *Bardasis-Schrieffer mode:* This mode represents a subdominant pairing channel that could be activated by pumping the SC state. Its excitation energy would be below the binding energy 2Δ of the dominant pairing channel and this mode would also not be subject to screening. Hence, these two arguments do not rule out this mode. However, the Bardasis-Schrieffer mode would leave a fingerprint on the Stokes side, as observed in pnictides.[48–50] We see no indication of this mode. Furthermore, it would be considered in our analysis, which uses the Stokes channel to calculate the anti-Stokes intensity. In order to explain the observation of a B_{1g} excitation energy below the A_{1g} excitation energy, a highly unconventional order parameter of the subdominant pairing mechanism would be required. This leaves the Higgs particle as the best explanation for the NEARS feature.

Conclusions

We have introduced NEARS that allows us to observe in-gap modes of A_{1g} and B_{1g} symmetry in the superconductor Bi-2212. By comparison between Stokes and anti-Stokes Raman data, other excitations of the superconductor such as quasi-particle excitations can be iden-

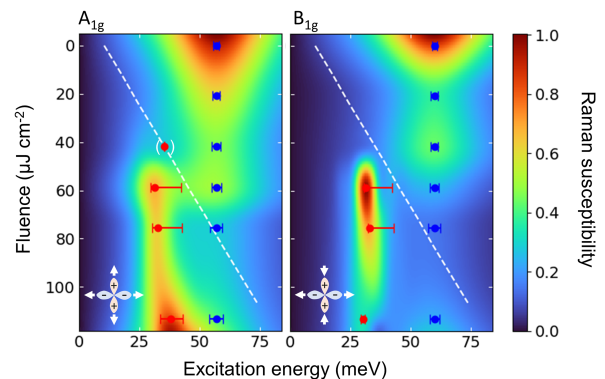


FIG. 3. Unified excitation spectrum of the superconductor Bi-2212. NEARS maps of Bi-2212. Raman cross section of the Higgs particle between 30 and 35 meV together with the pair-breaking excitation around 60 meV in A_{1g} (left) and B_{1g} (right) geometry at a time delay of 3 ps. The dashed white line marks the high-energy cutoff of the anti-Stokes energy window (see SI, Fig. S4 and S7). Raman energies obtained from the fit (and shown in Fig. 2) are shown as red and blue data points, respectively. The symmetry of the Higgs particle for the respective pump/probe configuration is indicated at the bottom left.

tified. This allows us to assign the observed modes to the Higgs particle. NEARS makes Higgs spectroscopy applicable to many materials classes characterized by the interplay of superconductivity and competing or co-existing orders.[49, 51–53] This technique goes beyond conventional Raman spectroscopy for the identification of the symmetry of SC order parameters. Higgs spectroscopy depends on both the symmetry of the quench and the symmetry of the Raman polarization probing the Cooper channel. Furthermore, we show that the fluence dependence of different symmetries allows to control the strength of the Higgs excitation. The energy and symmetry properties of the SC Higgs field are material-dependent and enable to study and control Higgs physics. Since the Meissner effect requires the presence of the Higgs field, the observation of a Higgs particle can serve as a novel criterion for superconductivity.

ACKNOWLEDGMENTS

The authors thank Lara Benfatto (Università di Roma “La Sapienza”), Roberto Merlin (University of Michigan), and Peter Abbamonte (University of Illinois Urbana-Champaign) for inspiring and productive discussions and input.

We acknowledge funding from Max Planck-UBC-UTokyo Center for Quantum Materials; Canada First Research Excellence Fund, Quantum Materials and Future Technologies Program; Natural Sciences and Engineering Research Council of Canada (NSERC); Canada Foundation for Innovation (CFI); Department

of National Defence (DND); British Columbia Knowledge Development Fund (BCKDF); Canada Research Chairs Program; CIFAR Quantum Materials Program; U.S. Department of Energy through the University of Minnesota Center for Quantum Materials, Grant No. DE-SC0016371; Bundesministerium für Bildung und Forschung via 05K19GU5 and 05K22GU2; and Funding by the European Union (ERC, T-Higgs, GA 101044657). (Views and opinions expressed are however those of the author(s) only and do not necessarily reflect those of the European Union or the European Research Council Executive Agency. Neither the European Union nor the granting authority can be held responsible for them.)

* tglier@physnet.uni-hamburg.de

† stefan.kaiser@tu-dresden.de

‡ d.manske@fkf.mpg.de

§ mruebhau@physnet.uni-hamburg.de

- [1] Nambu, Y. Quasi-particles and gauge invariance in the theory of superconductivity. *Phys. Rev.* **117**, 648 – 663 (1960). URL <https://doi.org/10.1103/PhysRev.117.648>.
- [2] Anderson, P. Coherent excited states in the theory of superconductivity: gauge invariance and the Meissner effect. *Phys. Rev.* **110**, 827 – 835 (1958). URL <https://doi.org/10.1103/PhysRev.110.827>.
- [3] Pekker, D. & Varma, C. M. Amplitude/Higgs modes in condensed matter physics. *Annual Review of Condensed Matter Physics* **6**, 269 – 297 (2015). URL <https://doi.org/10.1146/annurev-conmatphys-031214-014350>.
- [4] Higgs, P. Prehistory of the Higgs boson. *Comptes Rendus Physique* **8**, 970 – 972 (2007). URL <https://doi.org/10.1016/j.crhy.2006.12.006>.
- [5] Varma, C. M. Higgs boson in superconductors. *Journal of Low Temperature Physics* **126**, 901 – 909 (2002). URL <https://doi.org/10.1023/A:1013890507658>.
- [6] Schwarz, L. *et al.* Classification and characterization of nonequilibrium Higgs modes in unconventional superconductors. *Nat Commun* **11**, 287 (2020). URL <https://doi.org/10.1038/s41467-019-13763-5>.
- [7] Sooryakumar, R. & Klein, M. V. Raman scattering by superconducting-gap excitations and their coupling to charge-density waves. *Phys. Rev. Lett.* **45**, 660 – 662 (1980). URL <https://doi.org/10.1103/PhysRevLett.45.660>.
- [8] Feng, L. *et al.* Dynamical interplay between superconductivity and charge density waves: A nonlinear terahertz study of coherently driven 2H-NbSe₂. *Phys. Rev. B* **108**, L100504 (2023). URL <https://doi.org/10.1103/PhysRevB.108.L100504>.
- [9] Cea, T. & Benfatto, L. Nature and Raman signatures of the Higgs amplitude mode in the coexisting superconducting and charge-density-wave state. *Phys. Rev. B* **90**, 224515 (2014). URL <https://doi.org/10.1103/PhysRevB.90.224515>.
- [10] Littlewood, P. & Varma, C. Amplitude collective modes in superconductors and their coupling to charge-density waves. *Phys. Rev. B* **26**, 4883 – 4893 (1982). URL <https://doi.org/10.1103/PhysRevB.26.4883>.
- [11] Méasson, M.-A. *et al.* Amplitude Higgs mode in the 2H-NbSe₂ superconductor. *Phys. Rev. B* **89**, 060503 (2014). URL <https://doi.org/10.1103/PhysRevB.89.060503>.
- [12] Grasset, R. *et al.* Higgs-mode radiance and charge-density-wave order in 2H-NbSe₂. *Phys. Rev. B* **97**, 094502 (2018). URL <https://doi.org/10.1103/PhysRevB.97.094502>.
- [13] Chu, H. *et al.* Fano interference between collective modes in cuprate high-T_C superconductors. *Nat Commun* **14**, 1343 (2023). URL <https://doi.org/10.1038/s41467-023-36787-4>.
- [14] Matsunaga, R. *et al.* Light-induced collective pseudospin precession resonating with Higgs mode in a superconductor. *Science* **345**, 1145 – 1149 (2014). URL <https://doi.org/10.1126/science.1254697>.
- [15] Budelmann, D. *et al.* Gaplike Excitations in the Superconducting State of Bi₂Sr₂CaCu₂O₈ Studied by Resonant Raman Scattering. *Phys. Rev. Lett.* **95**, 057003 (2005). URL <https://doi.org/10.1103/PhysRevLett.95.057003>.
- [16] Saichu, R. P. *et al.* Two-Component Dynamics of the Order Parameter of High Temperature Bi₂Sr₂CaCu₂O_{8+δ} Superconductors Revealed by Time-Resolved Raman Scattering. *Phys. Rev. Lett.* **102**, 177004 (2009). URL <https://doi.org/10.1103/PhysRevLett.102.177004>.
- [17] Pellatz, N. *et al.* Relaxation timescales and electron-phonon coupling in optically pumped YBa₂Cu₃O_{6+x} revealed by time-resolved Raman scattering. *Phys. Rev. B* **104**, L180505 (2021). URL <https://doi.org/10.1103/PhysRevB.104.L180505>.
- [18] Han, S. *et al.* Incoherent phonon population and exciton-exciton annihilation dynamics in monolayer WS₂ revealed by time-resolved Resonance Raman scattering. *Optics Express* **27**, 29949 (2019). URL <https://doi.org/10.1364/OE.27.029949>.
- [19] Katsumi, K. *et al.* Higgs Mode in the d -Wave Superconductor Bi₂Sr₂CaCu₂O_{8+x} Driven by an Intense Terahertz Pulse. *Phys. Rev. Lett.* **120**, 117001 (2018). URL <https://doi.org/10.1103/PhysRevLett.120.117001>.
- [20] Chu, H. *et al.* Phase-resolved Higgs response in superconducting cuprates. *Nat Commun* **11**, 1793 (2020). URL <https://doi.org/10.1038/s41467-020-15613-1>.
- [21] Vaswani, C. *et al.* Light quantum control of persisting Higgs modes in iron-based superconductors. *Nat Commun* **12**, 258 (2021). URL <https://doi.org/10.1038/s41467-020-20350-6>.
- [22] Wang, Z.-X. *et al.* Transient Higgs oscillations and high-order nonlinear light-Higgs coupling in a terahertz wave driven NbN superconductor. *Phys. Rev. B* **105**, L100508 (2022). URL <https://doi.org/10.1103/PhysRevB.105.L100508>.
- [23] Reinhofer, C. *et al.* High-order nonlinear terahertz probing of the two-band superconductor MgB₂: Third- and fifth-order harmonic generation. *Phys. Rev. B* **106**, 214514 (2022). URL <https://doi.org/10.1103/PhysRevB.106.214514>.
- [24] Katsumi, K. *et al.* Revealing novel aspects of light-matter coupling in terahertz two-dimensional coherent spectroscopy: the case of the amplitude mode in superconductors. *preprint* (2023). URL <http://arxiv.org/abs/2311.16449>.
- [25] Shimano, R. & Tsuji, N. Higgs mode in superconductors. *Annu. Rev. Condens. Matter Phys.* **11**, 103 – 124 (2020). URL <https://doi.org/10.1146/>

- annurev-conmatphys-031119-050813.
- [26] Kim, M.-J. *et al.* Tracing the dynamics of superconducting order via transient third harmonic generation. *preprint* (2023). URL <https://arxiv.org/abs/2303.03288>.
- [27] Tsuji, N. & Aoki, H. Theory of Anderson pseudospin resonance with Higgs mode in superconductors. *Phys. Rev. B* **92**, 064508 (2015). URL <https://doi.org/10.1103/PhysRevB.92.064508>.
- [28] Hannibal, S. *et al.* Quench dynamics of an ultracold Fermi gas in the BCS regime: Spectral properties and confinement-induced breakdown of the Higgs mode. *Phys. Rev. A* **91**, 043630 (2015). URL <https://doi.org/10.1103/PhysRevA.91.043630>.
- [29] Schwarz, L. & Manske, D. Theory of driven Higgs oscillations and third-harmonic generation in unconventional superconductors. *Phys. Rev. B* **101**, 184519 (2020). URL <https://doi.org/10.1103/PhysRevB.101.184519>.
- [30] Benfatto, L., Castellani, C. & Seibold, G. Linear and nonlinear current response in disordered d-wave superconductors. *Phys. Rev. B* **108**, 134508 (2023). URL <https://doi.org/10.1103/PhysRevB.108.134508>.
- [31] Seibold, G., Udina, M., Castellani, C. & Benfatto, L. Third harmonic generation from collective modes in disordered superconductors. *Phys. Rev. B* **103**, 014512 (2021). URL <https://doi.org/10.1103/PhysRevB.103.014512>.
- [32] Udina, M. *et al.* Thz non-linear optical response in cuprates: predominance of the bcs response over the higgs mode. *Faraday Discussions* **237**, 168 – 185 (2022). URL <http://doi.org/10.1039/D2FD00016D>.
- [33] Sun, Z., Fogler, M. M., Basov, D. N. & Millis, A. J. Collective modes and terahertz near-field response of superconductors. *Phys. Rev. Res.* **2**, 023413 (2020). URL <https://doi.org/10.1103/PhysRevResearch.2.023413>.
- [34] Gabriele, F., Udina, M. & Benfatto, L. Non-linear Terahertz driving of plasma waves in layered cuprates. *Nat Commun* **12**, 752 (2021). URL <https://doi.org/10.1038/s41467-021-21041-6>.
- [35] Sellati, N., Gabriele, F., Castellani, C. & Benfatto, L. Generalized Josephson plasmons in bilayer superconductors. *Phys. Rev. B* **108**, 014503 (2023). URL <https://doi.org/10.1103/PhysRevB.108.014503>.
- [36] Barlas, Y. & Varma, C. M. Amplitude or higgs modes in d-wave superconductors. *Phys. Rev. B* **87**, 054503 (2013). URL <https://doi.org/10.1103/PhysRevB.87.054503>.
- [37] Eisaki, H. *et al.* Effect of chemical inhomogeneity in bismuth-based copper oxide superconductors. *Phys. Rev. B* **69**, 064512 (2004). URL <https://doi.org/10.1103/PhysRevB.69.064512>.
- [38] Munnikes, N. *et al.* Pair breaking versus symmetry breaking: Origin of the Raman modes in superconducting cuprates. *Phys. Rev. B* **84**, 144523 (2011). URL <https://doi.org/10.1103/PhysRevB.84.144523>.
- [39] Devereaux, T. P. & Einzel, D. Electronic Raman scattering in superconductors as a probe of anisotropic electron pairing. *Phys. Rev. B* **51**, 16336 – 16357 (1995). URL <https://doi.org/10.1103/PhysRevB.51.16336>.
- [40] Blumberg, G. *et al.* Observation of Leggett’s Collective Mode in a Multiband MgB₂ Superconductor. *Phys. Rev. Lett.* **99**, 227002 (2007). URL <https://doi.org/10.1103/PhysRevLett.99.227002>.
- [41] Maiti, S., Maier, T. A., Böhm, T., Hackl, R. & Hirschfeld, P. J. Probing the Pairing Interaction and Multiple Bardasis-Schrieffer Modes Using Raman Spectroscopy. *Phys. Rev. Lett.* **117**, 257001 (2016). URL <https://doi.org/10.1103/PhysRevLett.117.257001>.
- [42] Böhm, T. *et al.* Microscopic origin of Cooper pairing in the iron-based superconductor Ba_{1-x}K_xFe₂As₂. *npj Quant Mater* **3**, 48 (2018). URL <https://doi.org/10.1038/s41535-018-0118-z>.
- [43] Klein, M. *et al.* Resonance Raman study of 2Δ-gap like features in superconducting Bi-2212 and YBCO. *Journal of Physics and Chemistry of Solids* **67**, 298 – 301 (2006). URL <https://doi.org/10.1016/j.jpcs.2005.10.161>.
- [44] Schulz, B. *et al.* Fully reflective deep ultraviolet to near infrared spectrometer and entrance optics for resonance Raman spectroscopy. *Rev. Sci. Instrum.* **76**, 073107 (2005). URL <https://doi.org/10.1063/1.1946985>.
- [45] Bock, A. Laser heating of YBa₂Cu₃O₇ films in Raman experiments. *Phys. Rev. B* **51**, 15506 – 15518 (1995). URL <https://doi.org/10.1103/PhysRevB.51.15506>.
- [46] Peskin, M. & Schroeder, D. *An Introduction To Quantum Field Theory* (Taylor and Francis Group, 1995).
- [47] Zirnbauer, M. R. Particle-hole symmetries in condensed matter. *Journal of Mathematical Physics* **62** (2021). URL <https://doi.org/10.1063/5.0035358>.
- [48] Scalapino, D. J. & Devereaux, T. P. Collective d-wave exciton modes in the calculated Raman spectrum of Fe-based superconductors. *Phys. Rev. B* **80**, 140512 (2009). URL <https://doi.org/10.1103/PhysRevB.80.140512>.
- [49] Bardasis, A. & Schrieffer, J. R. Excitons and Plasmons in Superconductors. *Phys. Rev.* **121**, 1050 – 1062 (1961). URL <https://doi.org/10.1103/PhysRev.121.1050>.
- [50] Chubukov, A. V., Eremin, I. & Korshunov, M. M. Theory of Raman response of a superconductor with extended s-wave symmetry: Application to the iron pnictides. *Phys. Rev. B* **79**, 220501 (2009). URL <https://doi.org/10.1103/PhysRevB.79.220501>.
- [51] Wang, X. *et al.* Superconductivity at 5K in alkali-metal-doped phenanthrene. *Nat Commun* **2**, 507 (2011). URL <https://doi.org/10.1038/ncomms1513>.
- [52] Norman, M. R. The Challenge of Unconventional Superconductivity. *Science* **332**, 196 – 200 (2011). URL <https://doi.org/10.1126/science.1200181>.
- [53] Service, R. F. At last, room temperature superconductivity achieved. *Science* **370**, 273 – 274 (2020). URL <https://doi.org/10.1126/science.370.6514.273>.
- [54] Chiu, C.-K., Teo, J. C. Y., Schnyder, A. P. & Ryu, S. Classification of topological quantum matter with symmetries. *Rev. Mod. Phys.* **88**, 035005 (2016). URL <https://doi.org/10.1103/RevModPhys.88.035005>.

MATERIALS AND METHODS

Raman instrument

Spontaneous Raman measurements were performed on the UT-3 Raman spectrometer.[44] This triple-grated spectrometer is fully achromatic due to the use of reflective optics. Excellent stray light rejection is achieved via an entrance objective with a large numerical aperture of 0.5 in a Cassegrain-type design, small focal points due to aberration-free off-axis paraboloids in combination with bilateral slits of the pre-monochromator, and an additional relay-stage equipped with two monolateral slits for setting an asymmetric bandpass for Stokes- and anti-Stokes measurements. A beam block in the entrance objective blocks reflected and emitted light in an angle of 21.8° to the vertical (see Fig. S2). In this way, a low-frequency cutoff of less than 5 cm^{-1} can be achieved.[44] However, in the current experiment, the low-frequency cutoff is limited to the natural Fourier-broadening of the laser line of the pulsed laser source to approx. 80 cm^{-1} . We utilized a pulsed Ti:Sapphire laser system, Tsunami model HP fs 15 WP (Spectra Physics Lasers Inc., California) at a fundamental wavelength of 802 nm with a second harmonic generation (SHG) unit generating the probe wavelength of 401 nm. The pulse duration was $1.2 \pm 0.1 \text{ ps}$ monitored with an autocorrelator (APE GmbH, Berlin, Germany). The 401 nm and 802 nm beams were guided over two separate beam paths as shown in Figure S1. For time delay scans, a motorized delay line in the pump beam path was used. A $\lambda/2$ waveplate in the probe beam path allows symmetry-dependent studies. We have employed B_{1g} polarization by using crossed polarization and A_{1g} symmetry by parallel polarization between incident and scattered light with respect to the a and b axes in the CuO_2 planes. Neutral density filter units/wheels were used for fluence dependence. Figure S2 shows the details of the entrance objective consisting of four on-axis parabolic mirrors, which focuses the light into the first monochromator. Pump and probe beam reach the sample at an angle of 21.8° . By this, we apply a non-zero in-plane momentum to the sample, which causes symmetry breaking and activation of the Higgs mode in B_{1g} symmetry.

Transient Stokes and anti-Stokes Raman measurements

To characterize the beam spot size and shape and align the spatial overlap of the probe and the pump spot, a DFK 23GM021 industrial camera (The Imaging Source, Bremen, Germany) with a pixel size of $3.75 \mu\text{m}$ was positioned at the focal point of the entrance objective of the UT-3. We used a probe spot (401 nm) of $\text{FWHM} = 19.5 \mu\text{m} \times 11.1 \mu\text{m}$ (hor x ver) and a pump spot of $\text{FWHM} = 22.5 \mu\text{m} \times 16.9 \mu\text{m}$ (hor x ver). The applied probe power was $4.75 \pm 0.15 \text{ mW}$ resulting in a fluence of $35.08 \pm 1.15 \mu\text{J cm}^{-2}$ at a repetition rate of 80 MHz of the Tsunami system. For the pump, fluences of $20 \mu\text{J cm}^{-2}$ to $113 \mu\text{J cm}^{-2}$ were used (see Table S1 for details). In order to establish temporal overlap of the two pulses, an ultrafast diode UPD-50-UP (Alphas, Göttingen, Germany) was placed in the focal point of the entrance objective, where probe and pump beam were focused. A Picoscope 6402B by Pico Technology (Cambridgeshire, United Kingdom) was used to monitor the pulses and find rough temporal overlap. We then conducted reference measurements on highly oriented pyrolytic graphite (HOPG) by Alfa Aesar, Thermo Fisher Scientific (Massachusetts, USA), to calibrate the delay line. Probe-only, pump-probe, pump-only, and background measurements were taken one after the other with an integration time of 30 min each. In general, we conducted 3 repetitions per measurement to improve the signal-to-noise ratio and ensure stability over the measurement time. Stokes and anti-Stokes measurements were carried out with two different settings of the spectrometer bandpass and monolateral slits.

Sample

The investigated sample is an $Y_{0.08}$ -substituted Bi-2212 crystal with a T_c of 92 K (see Figure S3) with the nominal composition $\text{Bi}_{2.00}\text{Sr}_{2.00}\text{Ca}_{0.92}\text{Y}_{0.08}\text{Cu}_2\text{O}_{8+\delta}$. It is slightly underdoped as compared to $T_{c,\text{max}} = 96 \text{ K}$. The sample was annealed at 500°C in Argon. For more details on sample growth see previous work.[37] A continuous flow LHe Konti-Cryostat Spectro (CryoVac, Troisdorf, Germany) was utilized to cool the sample down to 8 K base temperature.

Data treatment

Raman spectra have been corrected for the static background detector signal and the spectral response of the spectrometer. The data was then normalized to the respective probe laser power and integration time. For NEARS

data, no Bose-function correction was applied to the data itself, since the division Bose factor for anti-Stokes spectra converges to zero (see Figure S4). We, therefore, plot the Raman intensity instead of the Raman susceptibility (see Figure 1 and 2 in the main text). However, by utilizing the linkage of Stokes and anti-Stokes data via the Bose-function (see equation S1), one can calculate the anti-Stokes spectrum from the measured Stokes spectrum, and analyze the difference between the calculated anti-Stokes and the measured anti-Stokes data. As a key result of this work, we find no difference signal for all non-pumped data and pump-probe data above T_c (see Fig. 1 in the main text). However, in the superconducting state and in the pump-probe measurement, we obtain a difference signal in the anti-Stokes data, which can be attributed to an inversion population of the excited Higgs state. NEARS maps are derived from the data by plotting the superposition of the Raman susceptibility of the in-gap NEARS feature obtained from anti-Stokes data together with the Raman susceptibility of the pair-breaking feature (Stokes side) in an interpolation 2D color plot as a function of excitation energy. For this, we utilize the python class `scipy.interpolate.interp2d`. In order to make this new representation of non-equilibrium Raman data more accessible to the reader, Figure S7 shows the Raman susceptibility of the NEARS feature on an energy-gain (anti-Stokes) axis, together with the superconductivity induced Raman susceptibility on the Stokes side (pair-breaking peak) on an energy-loss axis. The white dashed line marks the experimental cutoff of the anti-Stokes window, which we define at an energy, where the Bose-function reduces the Raman intensity to 10 %. This cutoff is proportional to the fluence, which is directly connected to the effective sample temperature T via the determined laser heating rate (see Fig. S8).

SUPPLEMENTARY INFORMATION

BCS-Dirac Correspondence

In the following, we elaborate on an analogy between the BCS- and Dirac Hamiltonian, which is repeatedly pointed out in the literature.[1, 3]

In natural units, the Dirac Lagrangian of relativistic Fermions in Weyl representation with the gamma matrices

$$\gamma^0 = \begin{pmatrix} 0 & \mathbb{1} \\ \mathbb{1} & 0 \end{pmatrix} \quad \text{and} \quad \gamma^i = \begin{pmatrix} 0 & \tau^i \\ -\tau^i & 0 \end{pmatrix} \quad \text{is} \quad \mathcal{L}^{\text{Dirac}} = \bar{\Psi} (i\cancel{\partial} - m) \Psi. \quad (\text{S1})$$

Legendre transformation using the canonical momentum $\frac{\delta \mathcal{L}}{\delta \partial_0 \Psi} = i\Psi^\dagger$ results in the Dirac-Hamiltonian[46]

$$H^{\text{Dirac}} = \Psi^\dagger (i\boldsymbol{\tau} \cdot \nabla \hat{\tau}_3 + m\hat{\tau}_1) \Psi = \begin{pmatrix} \Psi_L^\dagger & \Psi_R^\dagger \end{pmatrix} \begin{pmatrix} i\boldsymbol{\tau} \cdot \nabla & m \\ m & -i\boldsymbol{\tau} \cdot \nabla \end{pmatrix} \begin{pmatrix} \Psi_L \\ \Psi_R \end{pmatrix}. \quad (\text{S2})$$

Here we use $\hat{\tau}_i = \tau_i \otimes \mathbb{1}_{2 \times 2}$ to distinguish the extension of the Pauli matrices to 4×4 block matrices.

The eigenvalues of this Hamiltonian are $\pm E_{\mathbf{p}} = \pm \sqrt{\mathbf{p}^2 c^2 + m^2 c^4}$.

Using Nambu spinor notation the BCS-Hamiltonian (without local $U(1)$ symmetry i.e. uncharged BCS) may be rewritten into a Bogoliubov-deGennes Hamiltonian,

$$H^{\text{BdG}} = \sum_{\mathbf{k}} \Psi_{\mathbf{k}}^\dagger (\xi_{\mathbf{k}} \tau_3 + \Delta_{\mathbf{k}} \tau_1) \Psi_{\mathbf{k}} = \sum_{\mathbf{k}} \begin{pmatrix} \Psi_{\mathbf{k},\uparrow}^\dagger & \Psi_{-\mathbf{k},\downarrow} \end{pmatrix} \begin{pmatrix} \xi_{\mathbf{k}} & \Delta_{\mathbf{k}} \\ \Delta_{\mathbf{k}} & -\xi_{\mathbf{k}} \end{pmatrix} \begin{pmatrix} \Psi_{\mathbf{k},\uparrow} \\ \Psi_{-\mathbf{k},\downarrow}^\dagger \end{pmatrix}. \quad (\text{S3})$$

The BdG Hamiltonian's eigenvalues are $\pm E_{\mathbf{k}} = \pm \sqrt{\xi_{\mathbf{k}}^2 + \Delta_{\mathbf{k}}^2}$. Unless the electronic dispersion $\epsilon_{\mathbf{k}}$ is linear in momentum, $E_{\mathbf{k}}$ is not a Lorentz invariant dispersion of the quasi-particles. However, in the vicinity of the Fermi surface $|\xi_{\mathbf{k}}| \ll W$, the bandwidth, we may approximate $\xi_{\mathbf{k}} \approx v_F(|\mathbf{k}| - k_F)$. For s-wave symmetry ($\Delta_{\mathbf{k}} = \Delta$) one can make the analogy explicit by introduction of $m_\Delta = \frac{\Delta}{v_F^2}$ and obtains

$$E_{\mathbf{k}}^{\text{BCS}} = \sqrt{(|\mathbf{k}| - k_F)^2 v_F^2 + m_\Delta^2 v_F^4}, \quad (\text{S4})$$

resembling the Dirac Hamiltonian's relativistic dispersion relation with the speed of light replaced by the Fermi velocity v_F .

It is worth mentioning that the (Bogoliubov quasi-)particle-hole symmetry of the BdG-Hamiltonian, in contrast to that of the Dirac Hamiltonian, is only a formal one.[47] Ultimately, this is because in constructing the BdG-Hamiltonian one is doubling the Hilbert space $V \rightarrow W = V \oplus V^*$, for which the space of positive energy states

$W_+ = V_+ \oplus V_-^*$ and that of negative energy states $W_- = V_- \oplus V_+^*$ are always isomorphic (using the Fréchet-Riesz isomorphism). It is then easy to show, that h^{BdG} satisfies particle-hole symmetry independently of physical properties like the dispersion $\xi_{\mathbf{k}}$, gap Δ or whether $V_+ \simeq V_-$. In particular, this is also true for $\Delta = 0$. Therefore, this formal particle-hole symmetry is not due to superconductivity and should not be confused with a physical symmetry. On the contrary, it may be viewed as a constraint, enforcing the dependence between the Nambu spinors Ψ^\dagger and Ψ , which a Hamiltonian must satisfy to be a BdG-Hamiltonian.[54] The physical particle-hole symmetry mentioned in the context of superconductors is an approximate symmetry restricted to the states of energies $E \sim \Delta$ close to the Fermi surface. It is essentially just a consequence of Taylor expanding the density of states to zeroth order, which is often a sufficiently good approximation in conventional superconductors because $\Delta \ll W$.

Temperature calculation

Raman spectroscopy enables the determination of an effective sample temperature by the linking of Stokes and anti-Stokes spectra via the temperature-dependent Bose-function and thus makes a subtraction of laser-heating contributions from the original data possible. The identification of the effective temperature for every measurement was carried out using an algorithm based on the following equation:[45]

$$\frac{I_{AS}(\Delta E)}{I_S(\Delta E)} = \left(\frac{E_l + \Delta E}{E_l - \Delta E} \right)^4 \exp\left(-\frac{\Delta E}{k_B T}\right) \quad (S5)$$

I_{AS} and I_S describe the collected anti-Stokes and Stokes Raman intensities, E_l refers to the photon energy of the incident probe laser (3.09 eV in this study), ΔE is the Raman shift, k_B describes the Boltzmann constant, and T is the effective temperature. Fig. S8 (a) shows the measured Stokes data (blue) and anti-Stokes data (red) together with the Stokes data mirrored to the anti-Stokes side by equation S5 (black). The base temperature for this measurement was 293 K (room temperature), and an effective temperature of 302 K had to be considered to achieve agreement between Stokes and anti-Stokes spectra. This corresponds to a heating of 9 K for a probe laser power of 4.8 mW. Fig. S8 (b) shows the difference of Stokes and anti-Stokes integral as a function of heating for the exemplary measurement shown in (a) and defines the best estimate of the effective sample temperature as the minimum of the difference. To do this, we evaluate the integral difference in the energy region around two dominant phonons, as marked in Fig. S8 (a). For the heating caused by the pump, the fluence dependent data set was used to define a heating rate (K/mW). As shown in Fig. S8 (c), we find a heating rate of 3 ± 0.25 K/mW for the pump.

Data fitting procedure

Stokes spectra are described by the following fit function:

$$I_S = (n(\omega, T) + 1) \cdot \left[y_0 \cdot \tanh\left(\frac{\omega}{\omega_c}\right) + \frac{A_{2\Delta} \omega \Gamma_{2\Delta}}{(\omega^2 - \omega_{0,2\Delta}^2)^2 + \Gamma_{2\Delta}^2 \omega^2} + \sum_m \frac{A_m \omega \Gamma_m}{(\omega^2 - \omega_{0,m}^2)^2 + \Gamma_m^2 \omega^2} \right] \quad (S6)$$

where $(n(\omega, T) + 1)$ represents the thermal population factor (Bose-function):

$$n(\omega, T) + 1 = \frac{1}{\exp\left(\frac{\hbar\omega}{k_B T}\right) - 1} + 1 = \frac{1}{1 - \exp\left(-\frac{\hbar\omega}{k_B T}\right)} \quad (S7)$$

A background $y_0 \cdot \tanh\left(\frac{\omega}{\omega_c}\right)$ is used with the critical frequency ω_c . The phonons ($m = 9$) are fitted as Lorentzians, where A_m denotes the amplitude, Γ_m is the phonon damping, and $\omega_{0,m}$ is the phonon frequency of the m^{th} phonon. According to Ref [15], the pair-breaking peak is also modelled by a Lorentzian, with $A_{2\Delta}$ being the amplitude, $\Gamma_{2\Delta}$ the damping and $\omega_{0,2\Delta}$ corresponding to the gap energy.

To model the anti-Stokes spectra, phonon frequencies and widths, background, and pair-breaking feature are kept constant. The Bose-function changes from $(n(\omega, T) + 1)$ to $n(\omega, T)$. The phonon amplitudes as well as the Lorentzian NEARS feature representing a difference feature between Stokes and anti-Stokes was then fitted to the anti-Stokes data.

$$I_{\text{NEARS}} = n(\omega, T) \cdot \left(\frac{A_{\text{NEARS}} \omega \Gamma_{\text{NEARS}}}{(\omega^2 - \omega_{0,\text{NEARS}}^2)^2 + \Gamma_{\text{NEARS}}^2 \omega^2} \right) \quad (\text{S8})$$

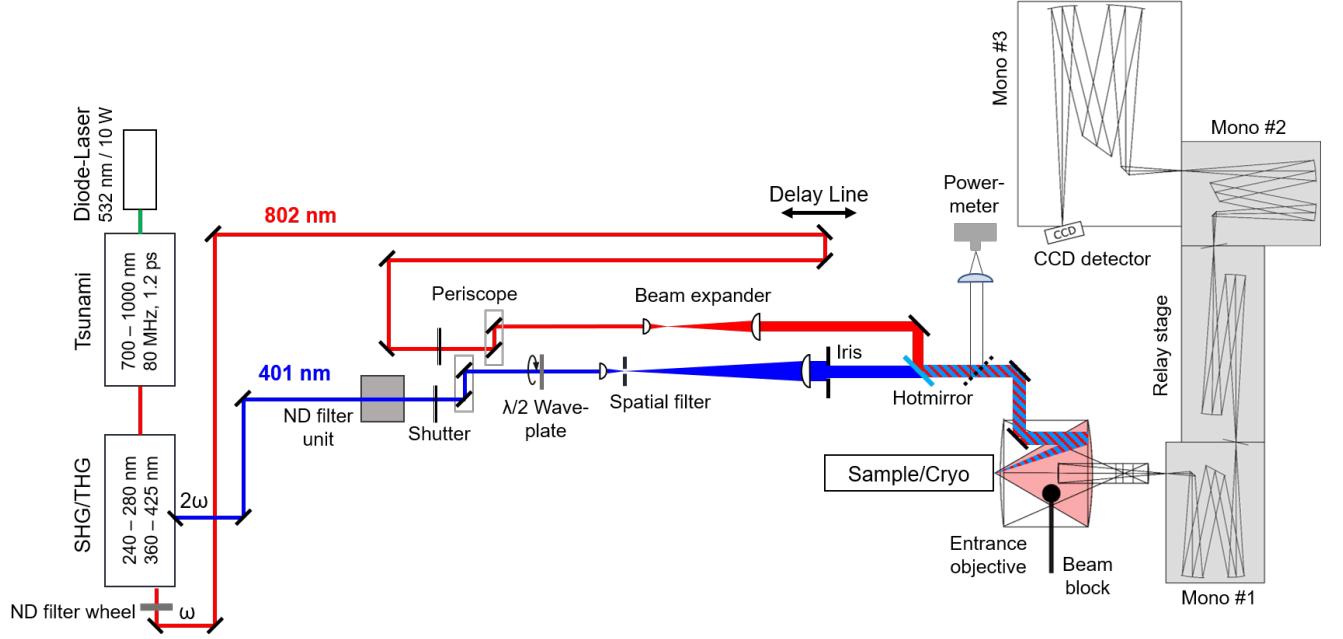


FIG. S1. Schematic view on the Raman setup. A Tsunami Ti:Sapphir system with a pulse duration of 1.2 ps and a repetition rate of 80 MHz is used as laser source at a fundamental wavelength of 802 nm (pump). From a second harmonic generation (SHG) unit, a 402 nm beam is used as the probe. The beam path includes ND filter units, shutters, a $\lambda/2$ waveplate to change the linear polarization of incidence light, a beam expander and spatial filter, a delay line for temporal overlap and scanning, and a hot mirror to overlay both beams. The entrance objective with its large numerical aperture of 0.5 is used to focus the light on the sample, and couples the Raman light into the first monochromator of the UT-3 spectrometer.[44] A beam block is used to block the specular reflex.

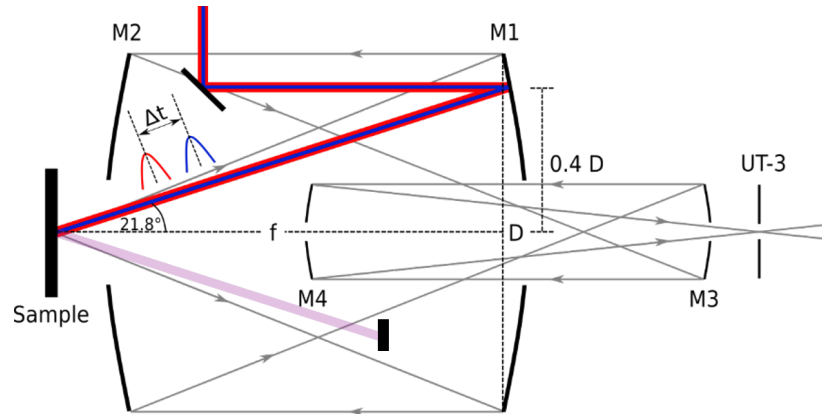


FIG. S2. Detailed view on the entrance objective of the UT-3. The Raman signal is collected with M1, collimated onto M2, which focuses the light in front of M3. This mirror collimates the light to provide a parallel beam section for the insertion of an analyzing beam cube. Pump and probe beam hit the sample with an angle of 21.8° to the vertical. By this, we apply a finite in-plane momentum to the sample, which causes symmetry breaking and activation of the Higgs mode in B_{1g} symmetry. A beam dump blocks the reflected light in 21.8° .

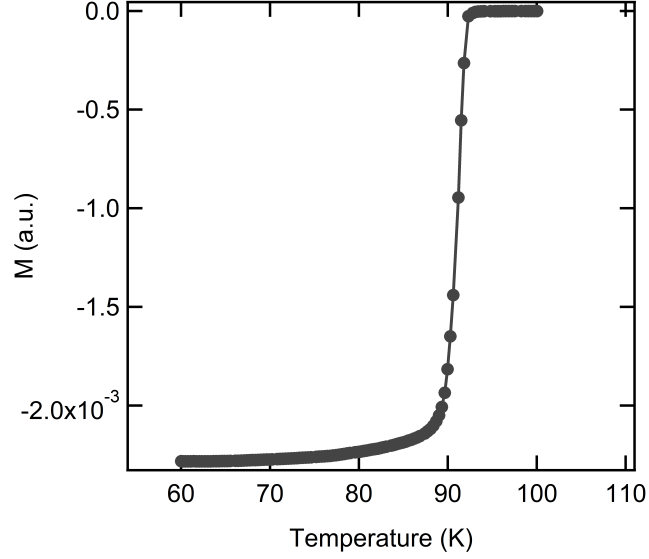


FIG. S3. Susceptibility curves of the measured Bi-2212 crystal with a T_c of 92 K.

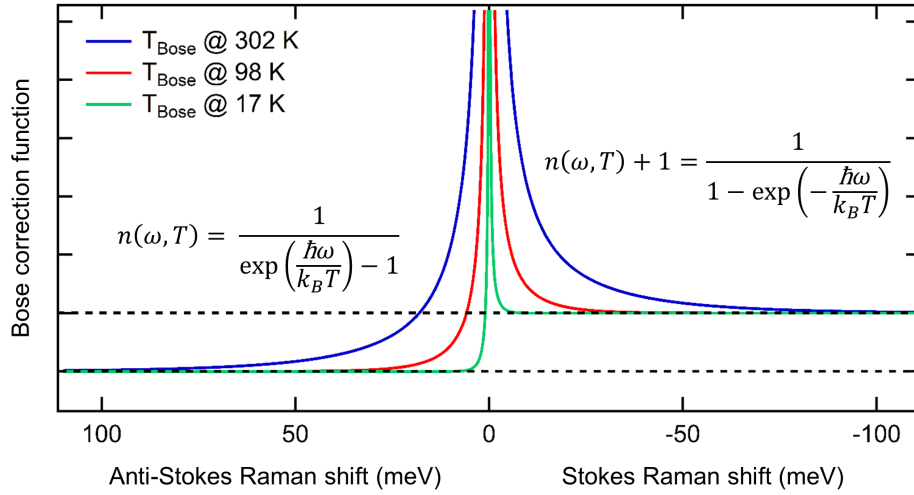


FIG. S4. Bose correction function for anti-Stokes Raman scattering ($n(\omega, T)$) and Stokes Raman scattering ($n(\omega, T) + 1$) for three exemplary temperatures. On the Stokes side, the Bose function converges to 1 for high energies, resulting in a non-zero Raman intensity. In comparison, on the anti-Stokes side, the Raman intensity aspires to become zero. Depending on the thermal population, an experimental observation window at low Raman shifts exists.

TABLE S1. Laser power, spot size, repetition rate and corresponding fluence for probe and pump.

	Laser Power	Spot Area	Rep. Rate	Fluence
Probe	4.75 ± 0.15 mW	169.23 ± 10.88 μm^2	80 MHz	35.08 ± 1.15 $\mu\text{J cm}^{-2}$
Pump	5.0 ± 0.1 mW	298.65 ± 19.19 μm^2	80 MHz	20.97 ± 0.93 $\mu\text{J cm}^{-2}$
	10.0 ± 0.1 mW	298.65 ± 19.19 μm^2	80 MHz	41.95 ± 2.27 $\mu\text{J cm}^{-2}$
	14.0 ± 0.1 mW	298.65 ± 19.19 μm^2	80 MHz	58.72 ± 3.35 $\mu\text{J cm}^{-2}$
	18.0 ± 0.1 mW	298.65 ± 19.19 μm^2	80 MHz	75.50 ± 4.43 $\mu\text{J cm}^{-2}$
	27.0 ± 0.1 mW	298.65 ± 19.19 μm^2	80 MHz	113.25 ± 6.86 $\mu\text{J cm}^{-2}$

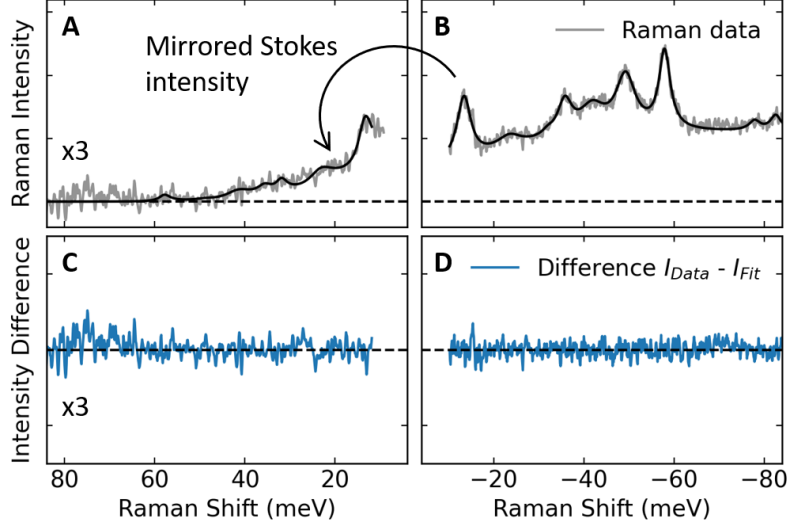


FIG. S5. Bi-2212 anti-Stokes (a) and Stokes (b) probe-only Raman intensity for B_{1g} geometry as a function of Raman shift at 100 K base temperature. The data is shown in grey. The black solid line represents a fit to the data, for which the Stokes Raman intensity (b) has been fitted as describes in equation S6. The Stokes intensity fit was then applied to the anti-Stokes side by using the anti-Stokes Bose function $n(\omega, T)$ instead of $n(\omega, T) + 1$. A temperature $T = 109$ K was used (100 K base temperature and 9 K probe heating, see SI). Phonon widths and frequencies were kept constant after fitting to the Stokes side. (c) and (d) show the difference between the data (grey) and the fit (red) shown in (a) and (b). The dashed line marks zero.

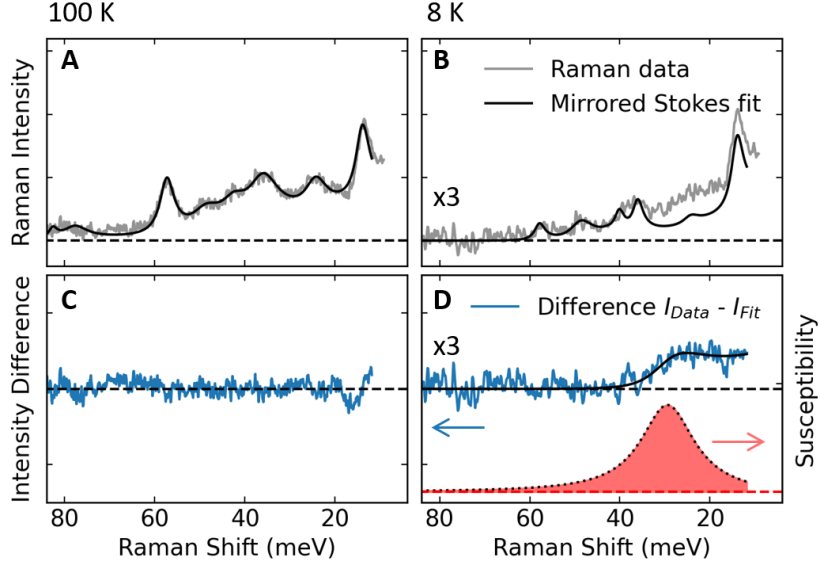


FIG. S6. (a) Pump probe Bi-2212 anti-Stokes Raman intensity for B_{1g} geometry as a function of Raman shift at 100 K base temperature. A pump fluence of $193 \mu\text{J cm}^{-2}$ was applied. The data is shown in grey. The black solid line represents a fit to the data, for which the corresponding Stokes Raman intensity has been fitted as describes in equation S6 and shown in Fig. S5. The Stokes intensity fit was then applied to the anti-Stokes side by using the Bose function $n(\omega, T)$ instead of $n(\omega, T) + 1$ and a temperature of 247 K (100 K base temperature, 9 K probe heating and (3 ± 0.6) K/mW pump heating rate, see SI). Phonon widths and frequencies were kept constant after fitting to the Stokes side. Please note the absence of any in-gap feature. (b) Pump probe Bi-2212 anti-Stokes Raman intensity for B_{1g} geometry as a function of Raman shift at 8 K base temperature. A pump fluence of $113 \mu\text{J cm}^{-2}$ was used. The effective temperature used within the Bose function is 98 K corresponding to the pump heating of (3 ± 0.6) K/mW and probe heating of 9 K. As shown in Fig. 2, we observe the pair-breaking feature even at our highest fluence of $113 \mu\text{J cm}^{-2}$ proving superconductivity. (c) Difference between the data (grey) and the fit (black) shown in (a) for the 100 K dataset. (d) Difference between the anti-Stokes data and the fit, which corresponds to the Stokes intensity, for the 8 K dataset. The black solid line represents a Lorentzian fit multiplied with the Bose function $n(\omega, T)$ to the NEARS feature. The red filled Lorentzian susceptibility is the susceptibility of the NEARS feature, as we show it in the main-text Figs. 1 and 2 and plot it in our NEARS map in Fig. 3 and Fig. S7.

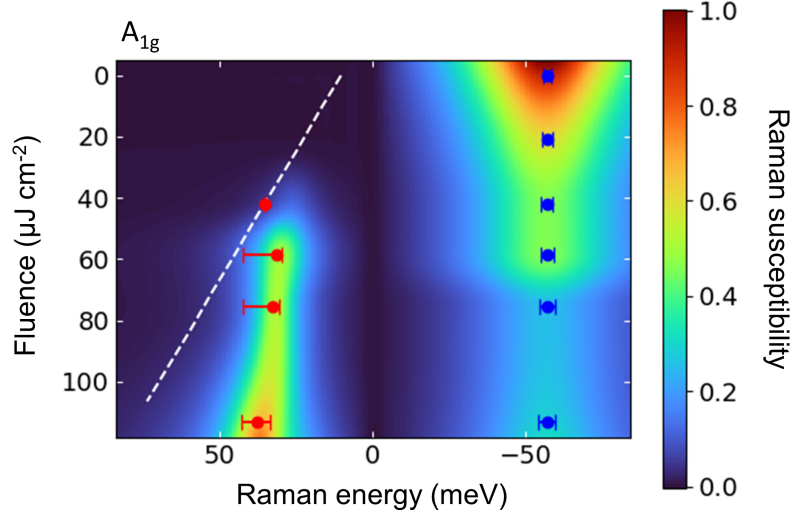


FIG. S7. Interpolated 2D color plot of the superconductivity-induced Raman susceptibilities obtained from the fit to the NEARS data in A_{1g} geometry. In the right (energy-loss) side, the pair-breaking feature from the Stokes data is shown. It decreases with increasing fluence. The blue data points represent the fit results (see Fig. 2 main text). On the left (energy-gain) side, one can observe the NEARS feature, representing the difference signal visible on the anti-Stokes side compared to the Stokes data. This difference signal can be identified, since Stokes and anti-Stokes data are linked via the Bose-function and, therefore, the Stokes data can be mirrored to the anti-Stokes side. The white dashed line represents the cutoff of the experimental observation window on the anti-Stokes side. In correspondence with our instrumental resolution, we determine this cutoff to be at a critical energy as a function of effective sample temperature, where the Bose-function $n(\omega, T)$ brings the Raman intensity down to 10 %. With this, we derive the NEARS map (see Fig. 3 main text) as a superposition of the two features as a function of absolute value of the Raman energy, corresponding to the excitation energy.

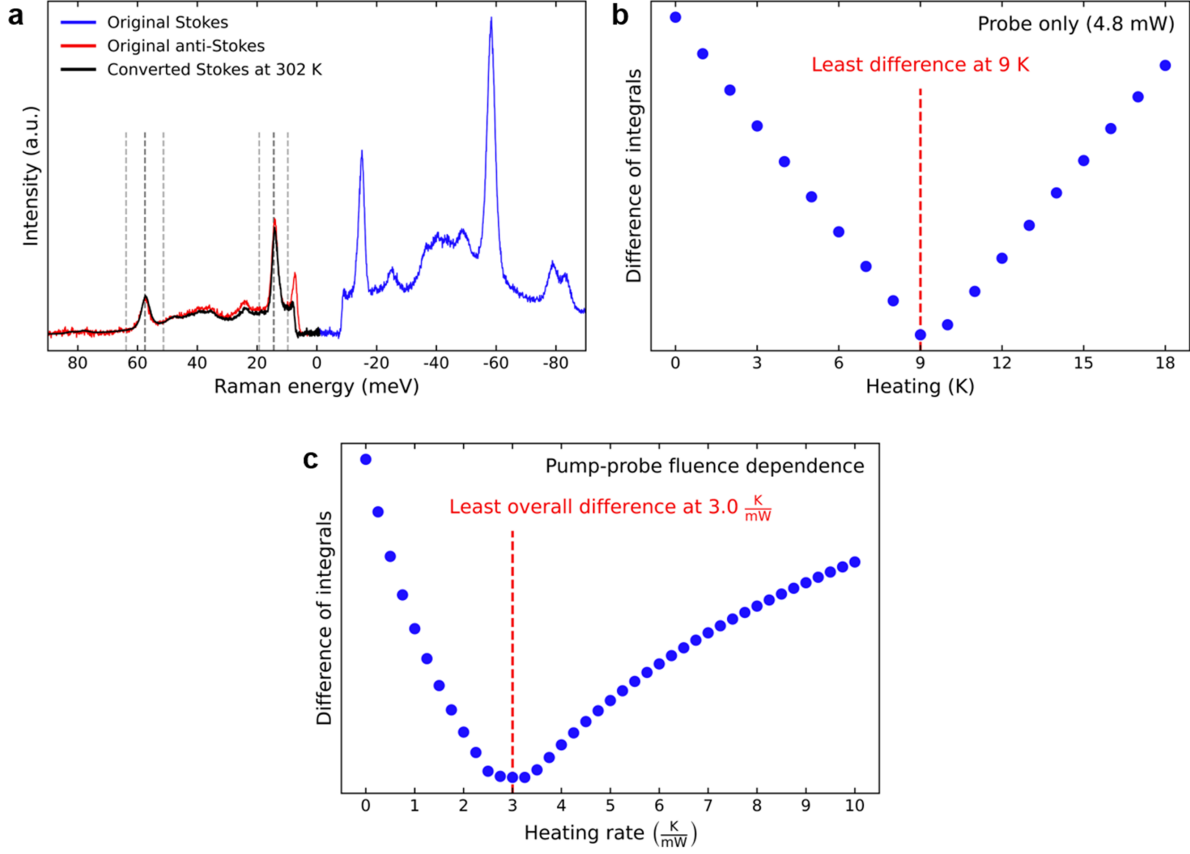


FIG. S8. (a) Converted probe-only Stokes spectrum (black) calculated from the original Stokes data (blue) according to eq. S5 at an effective temperature of 302 K (base temperature = 293 K). To determine the effective sample temperature of 302 K, the integral difference between the original anti-Stokes data (red) and the converted Stokes data around the dominant phonon modes for different temperatures was evaluated. Integral bounds are shown as light gray dashed lines and the locations used for determining the statistical weighing factor for the second integral are shown as dark gray dashed lines. (b) Difference of the integrals of original anti-Stokes data and converted Stokes data as introduced in (a) as a function of assumed heating for the probe-only data. The effective heating is equal to the difference between the temperature used to convert the Stokes data to the anti-Stokes side and the base temperature of 293 K. One can clearly identify a minimum at a heating of 9 K (302 K sample temperature). (c) Result of the algorithm performed on the entire series of fluence-dependent pump-probe measurements, showing a heating rate of 3 ± 0.25 K/mW for the pump.

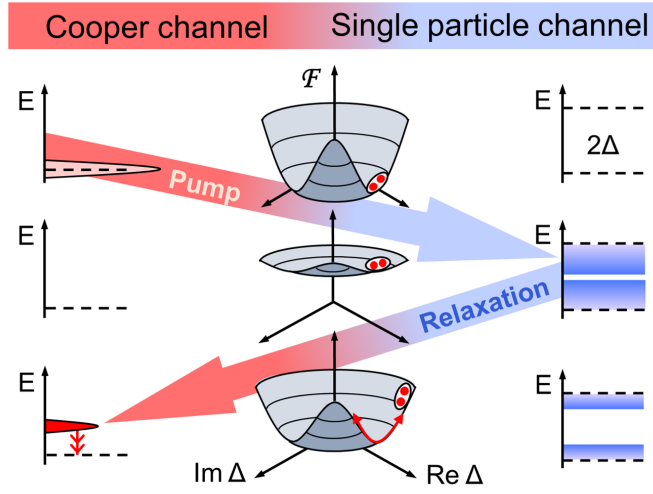


FIG. S9. Cooper channel vs. single-particle channel in the NEARS experiment on Bi-2212 highlighting the specific excitation process activating the Higgs mode in the NEARS channel. The Mexican-Hat potential representing the superconducting ground state is quenched upon pumping. Concomitantly, the reduction of the superfluid density and gap-filling occurs. On a time-scale of few ps the Mexican-Hat potential relaxes. The holes from the single-particle channel form again bosonic Cooper pairs, which oscillate in the relaxing Mexican-Hat potential representing an excited Higgs state. This population inversion is probed by NEARS leading to a strongly enhanced Raman susceptibility on the anti-Stokes side. It is important to note that this represents a three-level system in which the excited transient Higgs state has a higher population than the ground state leading to population inversion and a stronger anti-Stokes than Stokes response. This is only possible in superconductors due to the interplay between single-particle and Cooper channels. Conventional excitations such as phonons cannot show this behavior.